



UNIVERSIDAD NACIONAL AUTÓNOMA DE MÉXICO
POSGRADO EN CIENCIAS FÍSICAS
Óptica y Fotónica

TITULO QUE FALTA DEFINIR

PROTOCOLO DE INVESTIGACIÓN
QUE PARA OPTAR POR LA:
CANDIDATURA AL GRADO DE DOCTOR EN CIENCIAS (FÍSICA)

PRESENTA:
JONATHAN ALEXIS URRUTIA ANGUIANO

TUTOR:
DR. ALEJANDRO REYES CORONADO
FACULTAD DE CIENCIAS, UNAM

MIEMBROS DEL COMITÉ TUTOR
DR. RUBÉN RAMOS GARCÍA
INSTITUTO NACIONAL DE ASTROFÍSICA, ÓPTICA Y ELECTRÓNICA
DR. WOLF LUIS MOCHÁN BACKAL
INSTITUTO DE CIENCIAS FÍSICAS, UNAM

CIUDAD DE MÉXICO, MAYO DE 2025

Contents

1	Multiple Scattering Theories: two approaches	1
2	Results and Discussion	7
2.1	Supported and Totally Embedded Spherical Particles	7
2.1.1	Normal Incidence	8
	Conclusions	15

Multiple Scattering Theories: two approaches

The study of wave propagation in complex media has long been a central topic in optics, acoustics, and condensed matter physics. In particular, understanding the optical response of ensembles of nanoparticles (NPs) has garnered significant attention due to its relevance in fields such as nanophotonics, plasmonics, and metamaterials. Two main theoretical frameworks are typically employed to model these systems: Multiple Scattering Theories (MSTs) and Effective Medium Theories (EMTs).

The MSTs explicitly accounts for the interactions between individual scatterers and provides an accurate description of wave propagation in structured and disordered media [16, 21, 25]. The Foldy-Lax equations, formulated in the mid-20th century, offer a rigorous way to model the self-consistent field scattered by a collection of particles. In contrast, effective medium theories aim to replace a heterogeneous system with a homogeneous medium having equivalent macroscopic optical properties, often utilizing approximations such as Maxwell-Garnett and Bruggeman models. While EMTs offer computational simplicity and analytical tractability, they are generally less accurate since, they inherently neglect multiple scattering effects, phase coherence, and near-field coupling between NPs.

In the following sections, two main MSTs suited to describe the optical properties of ensembles of NPs constrained to a bidimensional

The Coherent Scattering Model (CSM), developed by Barrera and Valenzuela, is a theoretical framework designed to describe the optical response of disordered systems of scatterers. Unlike effective medium theories, which approximate heterogeneous media as homogeneous, the CSM is a multiple scattering approach that remains valid up to the quasicrystalline approximation (QSA). This model is particularly **relevant for dense collections of scatterers where coherent effects play a crucial role in the optical response** —Nel pastel.

Las teorías de esparcimiento múltiple (*Multiple Scattering Theories*, MSTs) resuelven, en el caso de esparcimiento de luz, las ecuaciones de Maxwell de forma aproximada cuando se ilumina un ensamble de partículas con una onda plana monocromática [16, 21, 25]. En particular, el Modelo de Esparcimiento Coherente (*Coherent Scattering Model*, CSM) es una MST que proporciona una expresión para los coeficientes de amplitud de reflexión y transmisión de la luz esparcida en la dirección coherente para un ensamble bidimensional desordenado de partículas esféricas [21, 26, 27]. En esta sección se presenta de forma breve en qué consisten las MSTs y se

enuncian las restricciones consideradas por el CSM.

En el esquema de las MSTs, la respuesta óptica de un arreglo desordenado de partículas arbitrarias, iluminado por una onda plana monocromática eléctrica incidente $\mathbf{E}^{\text{inc}}(\mathbf{r}, \omega)$ con frecuencia angular ω y dirección de propagación $\hat{\mathbf{k}}^{\text{inc}}$, está determinada por el campo eléctrico $\mathbf{E}_k^{\text{exc}}(\mathbf{r}, \omega)$ que excita a k -ésima partícula, de una colección de N , y que es igual a la suma del campo eléctrico incidente y el campo eléctrico inducido $\mathbf{E}_\ell^{\text{ind}}(\mathbf{r}, \omega)$ —el interno dentro de la partícula y el esparcido fuera de ésta— por los otros elementos del ensamble, es decir [26, 27]

$$\mathbf{E}_k^{\text{exc}}(\mathbf{r}) = \mathbf{E}^{\text{inc}}(\mathbf{r}) + \sum_{\ell \neq k}^N \mathbf{E}_\ell^{\text{ind}}(\mathbf{r}), \quad (1.1)$$

donde se obvia la dependencia armónica. Dado que todas las partículas son excitadas por la misma interacción, el campo eléctrico inducido en la ℓ -ésima partícula está dado por [26, 27]

$$\mathbf{E}_\ell^{\text{ind}}(\mathbf{r}) = \int d^3 r' \mathbb{G}(\mathbf{r}, \mathbf{r}') \int d^3 r'' \mathbb{T}(\mathbf{r}' - \mathbf{r}_\ell, \mathbf{r}'' - \mathbf{r}_\ell) \mathbf{E}_\ell^{\text{exc}}(\mathbf{r}''), \quad (1.2)$$

en donde \mathbf{r}_ℓ es la posición del centro de la ℓ -ésima partícula, $\mathbb{G}(\mathbf{r}, \mathbf{r}')$ es la función de Green diádica —solución a la ecuación de Helmholtz vectorial con el producto de la diádica unitaria y una delta de Dirac centrada en \mathbf{r}' como fuente [28]—, \mathbb{T} es el operador de transición, o matriz T , que relaciona de forma lineal el campo eléctrico esparcido de una partícula con el campo eléctrico que la excita [28], y las integraciones se realizan sobre un mismo volumen V , descrito por las posiciones \mathbf{r}' y \mathbf{r}'' , tal que el centro \mathbf{r}_ℓ de la ℓ -ésima partícula se localice dentro de V [26].

El campo eléctrico total $\mathbf{E}(\mathbf{r})$ es igual a la suma de $\mathbf{E}^{\text{inc}}(\mathbf{r})$ y las N contribuciones del campo eléctrico inducido $\mathbf{E}_\ell^{\text{ind}}(\mathbf{r})$ en cada partícula, el cual se calcula al resolver el sistema de N ecuaciones dadas por las expresiones anteriores. Al tratar el caso de un arreglo desordenado, se calcula el promedio configuracional del campo eléctrico total $\langle \mathbf{E}(\mathbf{r}) \rangle$, que considera la probabilidad de ocurrencia de cada una de las combinaciones en las que pueden localizarse los centros \mathbf{r}_ℓ de los elementos del ensamble [26, 27]:

$$\langle \mathbf{E}(\mathbf{r}) \rangle = \mathbf{E}^{\text{inc}}(\mathbf{r}) + \sum_{\ell=1}^N \langle \mathbf{E}_\ell^{\text{ind}}(\mathbf{r}) \rangle = \mathbf{E}^{\text{inc}}(\mathbf{r}) + \sum_{\ell=1}^N \left(\prod_{k=1}^N \int d^3 r_k \rho(\mathbf{R}) \mathbf{E}_\ell^{\text{ind}}(\mathbf{r}) \right), \quad (1.3)$$

con $\rho(\mathbf{R})$ la densidad de probabilidad de que el ensamble se encuentre en una configuración espacial específica dada por $\mathbf{R} = (\mathbf{r}_1, \mathbf{r}_2, \dots, \mathbf{r}_N)^T$. Al calcular el promedio configuracional de la Ec. (1.2) se obtiene la contribución promedio del campo eléctrico inducido en la ℓ -ésima partícula, que está dada en términos de las siguientes expresiones [26, 27]

$$\langle \mathbf{E}_\ell^{\text{ind}}(\mathbf{r}) \rangle = \int d^3 r' \mathbb{G}(\mathbf{r}, \mathbf{r}') \int d^3 r'' \int d^3 r_\ell \rho(\mathbf{r}_\ell) \mathbb{T}(\mathbf{r}' - \mathbf{r}_\ell, \mathbf{r}'' - \mathbf{r}_\ell) \langle \mathbf{E}_\ell^{\text{exc}}(\mathbf{r}'', \mathbf{R}) \rangle_\ell, \quad (1.4a)$$

$$\langle \mathbf{E}_\ell^{\text{exc}}(\mathbf{r}'', \mathbf{R}) \rangle_\ell = \prod_{\substack{k=1 \\ k \neq \ell}}^N \int d^3 r_k \rho(\mathbf{R} | \mathbf{r}_\ell) \mathbf{E}_\ell^{\text{exc}}(\mathbf{r}''), \quad (1.4b)$$

where $\rho(\mathbf{r}_\ell)$ is the probability density of finding the center of the ℓ -th particle within the volume

Fig. 1.1: Diagram of the particle ensemble considered in the CSM, consisting of a collection of N identical spherical particles of radius a whose centers are randomly located within the integration volume V : an infinite film centered at the plane $z = 0$ and of thickness d , which tends to zero to reproduce the case of a two-dimensional array. The system, embedded in a dielectric matrix, is illuminated by a monochromatic plane wave incident on the film at an angle θ .

V , and Eq. (1.4b) represents the configurational average of the excitation electric field $\mathbf{E}_\ell^{\text{exc}}$ for the ℓ -th particle, considering its fixed position in V , which is described by the conditional probability density $\rho(\mathbf{R}|\mathbf{r}_\ell)$. This expression can be further developed by substituting Eq. (1.1) into Eq. (1.4b) and following an analogous procedure, considering the index swaps $k \rightarrow \ell$ and $\ell \rightarrow m$, yielding

$$\langle \mathbf{E}_\ell^{\text{exc}}(\mathbf{r}'', \mathbf{R}) \rangle_\ell = \mathbf{E}^{\text{inc}}(\mathbf{r}'') + \sum_{\substack{m=1 \\ m \neq \ell}}^N \int d^3 r' \mathbb{G}(\mathbf{r}', \mathbf{r}'') \times \int d^3 r''' \int d^3 r_m \rho(\mathbf{r}_m) \mathbb{T}(\mathbf{r}' - \mathbf{r}_m, \mathbf{r}''' - \mathbf{r}_m) \langle \mathbf{E}_m^{\text{exc}}(\mathbf{r}'', \mathbf{R}) \rangle_{\ell, m}, \quad (1.5a)$$

$$\langle \mathbf{E}_m^{\text{exc}}(\mathbf{r}'', \mathbf{R}) \rangle_{\ell, m} = \prod_{\substack{n=1 \\ n \neq \ell, m}}^N \int d^3 r_n \rho(\mathbf{R}|\mathbf{r}_\ell, \mathbf{r}_m) \mathbf{E}_n^{\text{exc}}(\mathbf{r}''), \quad (1.5b)$$

where Eq. (1.5b) represents the configurational average of the excitation field $\mathbf{E}_m^{\text{exc}}(\mathbf{r}'')$ acting on the m -th particle, considering the conditional probability density $\rho(\mathbf{R}|\mathbf{r}_\ell, \mathbf{r}_m)$ that the system is in configuration \mathbf{R} with \mathbf{r}_ℓ and \mathbf{r}_m fixed [26, 27]. By continuing this process for all N spheres in the ensemble, a set of N equations known as the Foldy-Lax hierarchy [25] can be constructed. Solving this hierarchy enables the computation of the averaged electric field at \mathbf{r} , taking multiple scattering effects into account. The hierarchical equations can be truncated at different orders, reducing them to invertible systems of equations by applying approximations to how multiple scattering excites the elements of the ensemble.

To truncate the Foldy-Lax hierarchy and determine the total averaged electric field, the CSM imposes two approximations at different orders. First, the Single Scattering Approximation (SSA) is considered, reducing the Foldy-Lax hierarchy to a single equation to be solved by neglecting multiple scattering effects [26]. Specifically, in the SSA, Eq. (1.4b) is equated to the incident electric field $\mathbf{E}^{\text{inc}}(\mathbf{r})$ [25, 27]. The second approximation in the CSM is the Quasi-Crystalline Approximation (QSA), where the Foldy-Lax hierarchy is rewritten as a system of two equations by assuming that the configurational average for cases with one and two fixed particles is approximately equal, meaning that Eqs. (1.4b) and (1.5) are set equal [25, 26]. While the SSA is suitable for dilute disordered arrays, as it disregards multiple scattering, the QSA adapts to denser ensembles—up to a coverage fraction of 60% [25]—because, under this condition, the average with two fixed particles does not significantly differ from the average with one fixed particle due to the presence of the remaining particles [26].

Once the approximation orders have been determined to truncate the Foldy-Lax hierarchy, the CSM introduces a series of assumptions about the particle ensemble to solve the resulting system of equations for each approximation. In particular, the CSM considers that the particle ensemble consists of $N \gg 1$ identical spherical particles of radius a —immersed in a dielectric

medium called the matrix—whose centers \mathbf{r}_ℓ are within the integration volume V , which consists of an infinite film of thickness d centered at $z = 0$, with a uniform probability density $\rho(\mathbf{r}_\ell) = 1/V$, and assumes that the volume V_ℓ of each sphere is negligible compared to V [26]; a schematic of the system is shown in Fig. 1.1. Under these assumptions, the electric field induced by the ensemble particles in the SSA can be computed by substituting in Eq. (1.4) the dyadic Green function \mathbb{G} with its plane wave representation and performing the configurational average, along with the limit $d \rightarrow 0$ to consider the case of a two-dimensional array [26]. This procedure results in

$$\langle \mathbf{E}_{\text{SSA}}^{\text{ind}}(\mathbf{r}) \rangle = \begin{cases} -\alpha S_j(\pi - 2\theta) \exp(i\mathbf{k}_{\text{coh}}^{\text{r}} \cdot \mathbf{r}) \mathbf{E}^{\text{inc}}(\mathbf{r}), & z > 0, \\ -\alpha S(0) \exp(i\mathbf{k}_{\text{coh}}^{\text{t}} \cdot \mathbf{r}) \mathbf{E}^{\text{inc}}(\mathbf{r}), & z < 0, \end{cases} \quad \text{with} \quad \alpha = \frac{2\Theta}{x^2 \cos \theta}, \quad (1.6)$$

where θ is the incidence angle at which the incident plane wave illuminates the two-dimensional array, $S_j(\vartheta)$ are the elements of the Mie scattering matrix [29]—which depend on the refractive index of the matrix, the sphere, and its size—evaluated at ϑ , with $j = 1$ for s -polarization and $j = 2$ for p -polarization. The term Θ corresponds to the coverage fraction of the array, and $x = k^{\text{ind}} a$ is the size parameter with k^{ind} being the magnitude of the incident field wave vector propagating in the matrix [26, 27]. The elements $S_j(\vartheta)$ are evaluated at $\vartheta = \pi - 2\theta$ and $\vartheta = 0$ as they correspond to the coherent scattering directions given by the law of reflection and Snell's law, respectively. From Eq. (1.6), it is shown that under the SSA, the two-dimensional array of spherical particles scatters light primarily in coherent directions, as the diffuse components interfere destructively [26]. Consequently, reflection $r_{\text{SSA}}^{(j)}$ and transmission $t_{\text{SSA}}^{(j)}$ amplitude coefficients can be defined for the two-dimensional array similarly to the Fresnel coefficients, given by

$$r_{\text{SSA}}^{(j)}(\theta) = -\alpha S_j(\pi - 2\theta), \quad \text{and} \quad t_{\text{SSA}}^{(j)}(\theta) = 1 - \alpha S(0). \quad (1.7)$$

In the case of the QSA, the system of equations to be solved consists of Eqs. (1.4) and (1.5), considering that Eqs. (1.4b) and (1.5b) are equal. To solve this system of equations, the ensemble is assumed to have the same characteristics as in the SSA case and additionally that the surroundings of each sphere are identical on average [27]. Therefore, the system of equations can be solved by proposing the *ansatz*

$$\langle \mathbf{E}_\ell^{\text{exc}}(\mathbf{r}) \rangle_\ell = \mathbf{E}_{\text{r}}^{\text{exc}}(\mathbf{r}) \exp(i\mathbf{k}_{\text{coh}}^{\text{r}} \cdot \mathbf{r}) + \mathbf{E}_{\text{t}}^{\text{exc}}(\mathbf{r}) \exp(i\mathbf{k}_{\text{coh}}^{\text{t}} \cdot \mathbf{r}) \quad (1.8)$$

that is, in the CSM, it is assumed that $\langle \mathbf{E}_\ell^{\text{exc}}(\mathbf{r}) \rangle_\ell$ consists of a contribution from an electric field propagating in the coherent reflection direction, denoted as $\mathbf{E}_{\text{r}}^{\text{exc}}$, and another in the transmission direction, denoted by $\mathbf{E}_{\text{t}}^{\text{exc}}$ [27]. These coherent contributions behave according to the SSA [Eq. (1.6)], so each will have a reflected and transmitted component. The sum of these contributions determines the induced electric field under the QSA. Solving the system of equations and substituting in Eq. (1.9), the amplitude coefficients of reflection $r_{\text{CSM}}^{(j)}$ and transmission $t_{\text{CSM}}^{(j)}$ can be defined, considering multiple scattering [26, 27]. These coherent contributions behave according to the SSA [Eq. (1.6)], so each of them will have a reflected and a transmitted component. The sum of these contributions determines the induced electric field under the QSA,

whose expression is

$$\langle \mathbf{E}_{\text{QSA}}^{\text{ind}}(\mathbf{r}) \rangle = \begin{cases} -\alpha \left(S_j(0) \|\mathbf{E}_r^{\text{exc}}(\mathbf{r})\| + S(\pi - 2\theta) \|\mathbf{E}_t^{\text{exc}}(\mathbf{r})\| \right) \exp(i\mathbf{k}_{\text{coh}}^r \cdot \mathbf{r}) \hat{\mathbf{E}}^{\text{inc}}, & z > 0, \\ -\alpha \left(S_j(\pi - 2\theta) \|\mathbf{E}_r^{\text{exc}}(\mathbf{r})\| + S(0) \|\mathbf{E}_t^{\text{exc}}(\mathbf{r})\| \right) \exp(i\mathbf{k}_{\text{coh}}^t \cdot \mathbf{r}) \hat{\mathbf{E}}^{\text{inc}}, & z < 0, \end{cases} \quad (1.9)$$

where $\hat{\mathbf{E}}^{\text{inc}}$ indicates the polarization of the incident electric field. Since in the QSA the expressions of Eq. (1.5) are equal for the electric field exciting a particle, then the contributions of the induced field in the coherent direction satisfy [27]

$$\mathbf{E}_r^{\text{exc}}(\mathbf{r}) = -\frac{\alpha}{2} \left(S_j(0) \|\mathbf{E}_r^{\text{exc}}(\mathbf{r})\| + S(\pi - 2\theta) \|\mathbf{E}_t^{\text{exc}}(\mathbf{r})\| \right) \hat{\mathbf{E}}^{\text{inc}}, \quad (1.10a)$$

$$\mathbf{E}_t^{\text{exc}}(\mathbf{r}) = \mathbf{E}^{\text{inc}}(\mathbf{r}) - \frac{\alpha}{2} \left(S_j(\pi - 2\theta) \|\mathbf{E}_r^{\text{exc}}(\mathbf{r})\| + S(0) \|\mathbf{E}_t^{\text{exc}}(\mathbf{r})\| \right) \hat{\mathbf{E}}^{\text{inc}}. \quad (1.10b)$$

Solving the system of equations for $\mathbf{E}_r^{\text{exc}}(\mathbf{r})$ and $\mathbf{E}_t^{\text{exc}}(\mathbf{r})$ shown in Eq. (1.10), and substituting them in Eq. (1.9), expressions for the reflection $r_{\text{CSM}}^{(j)}$ and transmission $t_{\text{CSM}}^{(j)}$ amplitude coefficients are defined, considering multiple scattering. These expressions are [26, 27]

$$r_{\text{CSM}}^{(j)}(\theta) = \frac{-\alpha S_j(\pi - 2\theta)}{1 + \alpha S(0) + \frac{1}{4}\alpha^2 [S^2(0) - S_j^2(\pi - 2\theta)]}, \quad (1.11a)$$

$$t_{\text{CSM}}^{(j)}(\theta) = \frac{1 - \frac{1}{4}\alpha^2 [S^2(0) - S_j^2(\pi - 2\theta)]}{1 + \alpha S(0) + \frac{1}{4}\alpha^2 [S^2(0) - S_j^2(\pi - 2\theta)]}, \quad (1.11b)$$

where $j = 1$ for s -polarization and $j = 2$ for p -polarization. The assumption that spherical particles are identical, imposed in both the SSA and QSA, can be relaxed if the radius a of the particles follows a size distribution density $\rho(a)$ and the field exciting each sphere is identical for all, except for a phase difference of $\pm 2ik_z^{\text{inc}}a$ caused by size variation [20]. In this case, the average over the particle radius a is computed in Eq. (1.10), incorporating the phase difference by multiplying the right-hand side of Eq. (1.10) by $\exp(\pm 2ik_z^{\text{inc}}a)$ —with $k_z^{\text{ind}} = k^{\text{ind}} \cos \theta$, where the positive sign corresponds to the reflected contribution and the negative to the transmitted one. Following the analogous procedure described earlier, the reflection and transmission amplitude coefficients considering size polydispersity in the two-dimensional array are given by [20].

$$r_{\text{CSM}}^{(j)}(\theta) = \frac{-\beta_+^{(j)}(\theta)}{1 + \beta_F + \frac{1}{4} [\beta_F^2 - \beta_+^{(j)}(\theta) \beta_-^{(j)}(\theta)]}, \quad (1.12a)$$

$$t_{\text{CSM}}^{(j)}(\theta) = \frac{1 - \frac{1}{4} [\beta_F^2 - \beta_+^{(j)}(\theta) \beta_-^{(j)}(\theta)]}{1 + \beta_F + \frac{1}{4} [\beta_F^2 - \beta_+^{(j)}(\theta) \beta_-^{(j)}(\theta)]}, \quad (1.12b)$$

where

$$\beta_F(\theta) = \eta \int_0^\infty \rho(a) S(0) da \quad \text{y} \quad \beta_\pm^{(j)}(\theta) = \eta \int_0^\infty \rho(a) S_j(\pi - 2\theta) \exp(\pm 2ik_z^{\text{inc}}a) da, \quad (1.13)$$

with $\eta = 2\Theta/(x_0^2 \cos \theta)$ and where $x_0 = k^{\text{ind}} a_0$ is the size parameter of a sphere with radius a_0 , which is the most probable value according to the size distribution density $\rho(a)$.

The expressions in Eq. (1.12) allow describing the response of a disordered metasurface of spherical NPs under conditions close to experimental ones by introducing the presence of a substrate. To achieve this, multiple reflections between the substrate-matrix interface and the matrix-metasurface interface are considered, assuming that the latter responds according to Eq. (1.12) when separated from the substrate by a distance $\Delta \rightarrow 0$ [20]. In particular, to compare the theoretical response with reflectance measurements in an internal incidence scheme, the amplitude reflection coefficient of the entire system (metasurface with substrate) is given by [20]

$$r^{(j)}(\theta_i) = \frac{r_{\text{sm}}^{(j)}(\theta_i) + r_{\text{CSM}}^{(j)}(\theta_t)}{1 + r_{\text{sm}}^{(j)}(\theta_i)r_{\text{CSM}}^{(j)}(\theta_t)}, \quad (1.14)$$

where r_{sm} is the Fresnel reflection coefficient between the substrate and the matrix for s (p) polarization if $j = 1$ ($j = 2$), and where θ_i is the angle of incidence of the plane wave illuminating the interface between the substrate and the matrix, and θ_t is the transmission angle upon crossing this interface and thus the angle at which it illuminates the metasurface.

Results and Discussion

2.1 Supported and Totally Embedded Spherical Particles

To compare the optical response of a NP in the presence of a substrate with that of a NP in a totally homogeneous environment, let us first analyze the spectral response given by the Mie Theory when the matrix and the size of the NP varies. In Fig. 2.1 it is shown the wavelength of resonance λ_{res} , that is, the wavelength at which the scattering (orange) and extinction (black) efficiencies are maximized, as a function of the radius a of a AuNP embedded in a matrix of air [Fig. 2.1a)] and of glass [Fig. 2.1b)], with a refractive index of $n_{\text{m}} = 1$ and $n_{\text{m}} = 1.5$, respectively, and as a function of the refractive index of the matrix n_{m} for a AuNP with a radius of $a = 12.5$ nm [Fig. 2.1c)] and with a radius of $a = 50$ nm [Fig. 2.1d)]. For the optical response of the AuNP it was employed the experimental data as reported by Johnson and Christy [30] (filled circles) and by considering a size correction —see Appendix ??— to it (empty circles).

From the results shown in Fig. 2.1 it can be seen that the wavelength of resonance λ_{res} for the extinction, considering the bulk dielectric function for Au (filled circles), is smaller than that of the scattering and that the distance between them decreases as either the size of the AuNP or the refractive index of the matrix increases. This behavior arises from a redshift of λ_{res} for increasing values of a and n_{m} and it shows that, for particles small compared to the wavelength of the incident light in the matrix, the main contribution to the extinction of light is due to absorption processes and as the size of the AuNP grows, the extinction is dominated by its other contribution: the scattering, as discussed in Section ?? and supported by Eq. (??). The redshift of λ_{res} can also be observed when considering a size corrected dielectric function (empty circles). Remarkably, for values of radius $\lesssim 15/n_{\text{m}}$ there is a blueshift of λ_{res} , as it can be seen in Figs. 2.1a) and 2.1b), which is a consequence of a greater imaginary part of the dielectric function for the AuNP due to the size correction. On the other hand, an increase in n_{m} for a fixed radius presents only redshifts either with or without a size corrected dielectric function [see Figs. 2.1c) and 2.1d)].

The spectral behavior of the scattering and extinction of light due to a spherical NP summarized in Fig. 2.1 was calculated by assuming a homogeneous medium (the matrix) where the NP is embedded and thus allowing the direction of the illuminating plane wave to be arbitrary, yet yielding the same results. In the following Sections, the homogeneity of the surroundings of the NP is substituted by two semiinfinite media and thus modifying the optical response of the

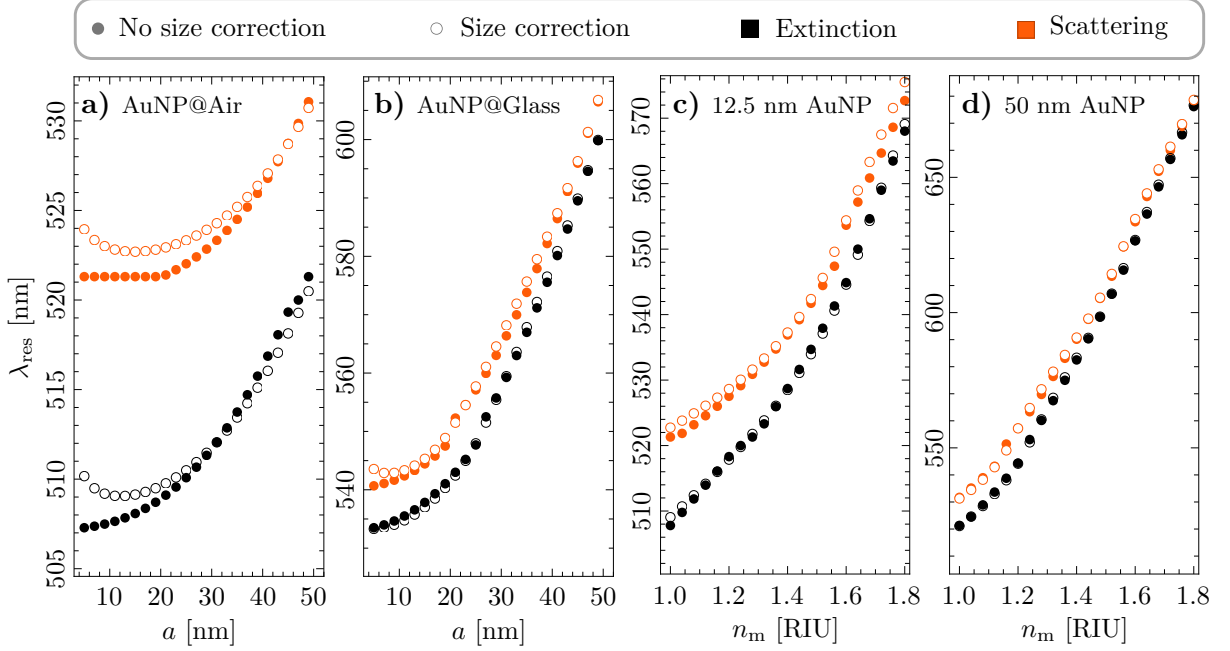


Fig. 2.1: Resonance wavelength λ_{res} of the scattering (orange) and extinction (black) efficiencies of a AuNP as a function of the NP’s radius when embedded **a)** in air ($n_m = 1$) and **b)** in glass ($n_m = 1.5$), and as a function of the refractive index of the matrix n_m for a AuNP of radius **c)** 12.5 nm and **d)** 50 nm, using the dielectric function for gold as reported by Johnson and Christy [30] (filled circles) and considering a size correction to it (empty circles).

system depending on how it is illuminated.

2.1.1 Normal Incidence

The problem of scattering and absorption of light by single spherical NP embedded in a matrix, with refractive index n_m , illuminated by a plane wave with wavelength λ and traveling in the \mathbf{k}^i direction, has spherical symmetry, which was exploited to develop the Mie Theory as explained in Section ???. If a substrate, with refractive index n_s , is considered and the NP is located right above or below the interface—without crossing the substrate-matrix interface—, there are four combinations in which the system can be excited since the NP can be either embedded in the substrate or supported on it, and it can be illuminated either in an external—from the matrix to the substrate—or in an internal—from the substrate to matrix— configuration, as shown in Fig. 2.2a), where the following cases are depicted: Embedded-External (EE), Embedded-Internal (EI), Supported-External (SE) and Supported-Internal (SI). In the presence of the substrate, the electric field illuminating the AuNP is not the incoming plane wave but the sum of it with the reflected electric field (EI and SE) or the transmitted electric field (EE and SI), both of which can be calculated analytically through Fresnel’s reflection and transmission amplitude coefficients, as discussed in Appendix ??.

In Figs. 2.2b) and 2.2c) the absorption Q_{abs} and scattering Q_{sca} efficiencies are shown, respectively, as a function of λ for a AuNP of radius $a = 12.5$ nm in the Embedded-External

2.1 Supported and Totally Embedded Spherical Particles

(black), Embedded-Internal (orange), Supported-External (blue) and Supported-Internal (light orange) configurations; the green shaded regions correspond to the values between the two limiting cases given by the Mie theory: the AuNP embedded in air (lower boundary) and embedded in glass (upper boundary). The magenta markers correspond to the values of the efficiencies evaluated at the wavelength of resonance considering the presence of a substrate while the cyan markers correspond to the efficiencies at the resonance wavelength for the Mie-limiting cases.

From the results shown in Figs. 2.2b) and 2.2c), it can be seen that both the absorption and scattering efficiencies of the four spatial configurations are of the same order of magnitude as the Mie-limiting cases and, even more, the values of the efficiencies for the embedded AuNP (black and orange lines) lie very close to the Mie-limiting case of the AuNP in glass (upper boundary of the green shaded region) and the same behavior is observed for the supported AuNP (blue and light orange lines) and the Mie-limiting case of a AuNP embedded in air (lower boundary of the green shaded region). The presence of a substrate yields an overall enhancement and damping of the scattering and the absorption efficiencies relative to the isolated NP, which depend on the illumination of the system since Q_{abs} and Q_{sca} are inversely proportional to the refractive index of the medium of incidence [Ecs. (??) and (??)]: If the system is illuminated in an external configuration, the obtained efficiencies are slightly decreased relative to the Mie-limiting case as it can be seen from the black and blue curves, which correspond to the EE and SE cases; on the other hand, the calculated efficiencies for the internal illuminated cases, that is for EI (orange) and SI (light orange), are enhanced relative to the Mie-limiting cases.

Another effect of the substrate in the optical response of the system is a slightly spectral shift of the excitation wavelength of the scattering and absorption efficiencies, which depends on the medium where the AuNP is located. For example, in Figs. 2.2b) and 2.2c) the wavelength of

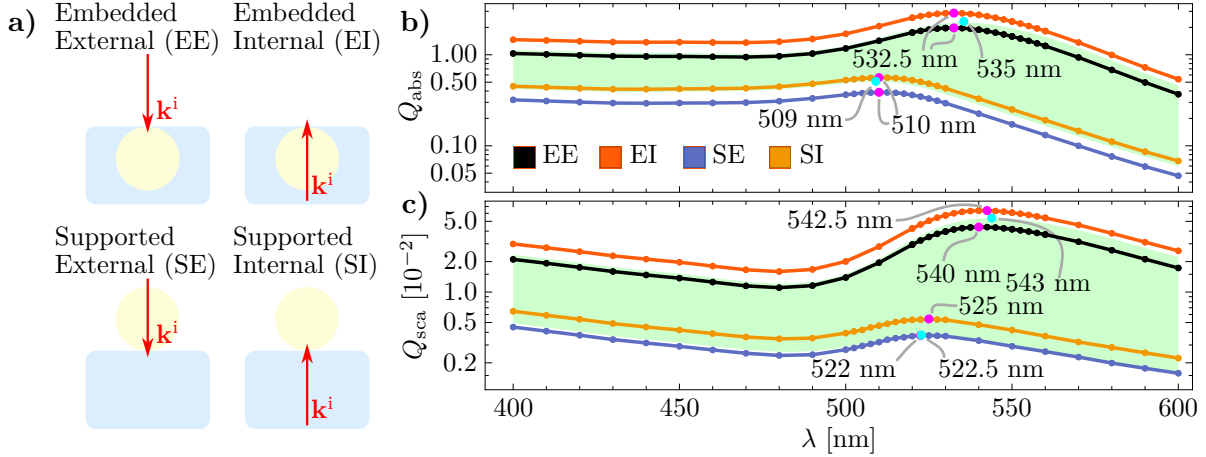


Fig. 2.2: a) Schematics of a AuNP embedded (E) in [supported (S) on] a glass substrate ($n_s = 1.5$) forming a planar interface with an air matrix ($n_m = 1$) and illuminated by a plane wave traveling normally to the air-glass interface in an external (E) and in an internal (I) configuration. b) Absorption Q_{abs} and c) scattering Q_{sca} efficiencies of a 12.5 nm AuNP as a function of the wavelength λ of the illuminating plane wave in different spatial configurations: EE (black), EI (orange), SE (blue) and SI (light orange). The green shaded region shows the two Mie-limiting cases of a AuNP embedded in air and in glass; the magenta (AuNP and substrate) and cyan (Mie-limiting) markers correspond to the efficiencies evaluated at the wavelength of resonance for each case.

2. RESULTS AND DISCUSSION

resonance for both the absorption and the scattering efficiencies (magenta markers) are redshifted ~ 1 nm, relative to the Mie-limiting case (cyan markers), for the AuNP supported on the substrate (blue and light orange curves) and blueshifted ~ 2 nm for the embedded AuNP (black and orange curves). These spectral shifts can be understood by considering the AuNPs as electric point dipoles parallel to the interface—an assumption consistent with the near-field distribution in the Mie-limiting cases and with the radiation patterns (see Figs. ?? and ??)—and their interaction with the image electric point dipoles induced within the substrate [31]. Both the dipoles induced in the AuNP and the image dipoles are parallel to the interface but its strength differs by a factor of $A_{\text{dip}} = (\sqrt{n_j} - \sqrt{n_i})/(\sqrt{n_j} + \sqrt{n_i})$ [16], where n_j is the refractive index of the medium where the real dipole (the AuNP) is located and n_i of the medium where the image dipole is induced. If the AuNP is embedded in the substrate, then $A_{\text{dip}} > 0$ meaning that the induced dipole is parallel to the real dipole, which is a more energetic configuration that yields the spectral blueshift of the resonance. Conversely, if the AuNP is supported on the substrate then $A_{\text{dip}} < 0$ and the induced dipole is antiparallel to the real dipole, leading to a less energetic configuration and to the redshift observed in Figs. 2.2b) and 2.2c).

The absorption and scattering efficiencies are integral quantities which describe the global behavior of the induced electric field \mathbf{E}^{ind} , which corresponds to the internal electric field \mathbf{E}^{int} inside the AuNP and to the scattered electric field \mathbf{E}^{sca} outside of it. The distribution of \mathbf{E}^{ind} , for a fixed wavelength, is studied in two spatial regimes: the far- and the near-field. To analyze the optical response in the first regime, the radiation patterns of the AuNP are obtained numerically by plotting the magnitude of the scattered electric field in the far-field regime¹ $\mathbf{E}_{\text{far}}^{\text{sca}}$ as a function of the angle relative to the normal direction to the interface. In Figs. 2.3 and 2.4, it is shown the radiation patterns of the embedded and the supported AuNP, respectively, for several values of the wavelength λ of the incident plane wave, as well as considering an illumination of the system in an [a) and b)] external and in an [c) and d)] internal configuration; additionally, it is considered that the incident electric field is totally [a) and c)] parallel to the scattering plane $\mathbf{E}_{\parallel}^{\text{i}}$ and [b) and d)] perpendicular to the scattering plane $\mathbf{E}_{\perp}^{\text{i}}$.

The radiation patterns of both the embedded and the supported AuNP follow the same trend independently of the illuminating wavelength λ but the amplitude is modulated by the scattering efficiencies shown in Fig. 2.2c). For example, in the EE and EI cases (Fig. 2.3) the scattered electric field (in the far-field) decreases its amplitude as the wavelength increases from 400 nm to 480 nm (black, orange and blue curves) and from 550 nm to 600 nm, while it increases from 485 nm to 542 nm, near the wavelength of resonance for the scattering efficiency, see Fig. 2.2c). Similarly, for the SE and SI cases the amplitude of the far-field is modulated by its scattering efficiency as it can be seen from comparing the radiation patterns in Fig. 2.4 at 400 nm (black), 480 nm (blue) and 527 nm (purple), with the value of Q_{sca} at those wavelengths corresponding to a global maximum, a global minimum and a local maximum at the wavelength

¹The FEM returns the induced electric field by a scatterer in a neighborhood around it and there is no guarantee that the returned electric field, even at the boundaries of the volume where the FEM simulation is performed, corresponds to the far-field regime. To calculate the radiation pattern from the obtained induced electric field, COMSOL Multiphysics™ Ver. 5.4 employs the Stratton-Chu formula [32], which is a near-field to far-field transformation that propagates the known electric near-field over a mathematical surface surrounding all the scatterers to an arbitrary point [33]. The Stratton-Chu formula is obtained by employing the vectorial generalization of the Green's second identity with the electric and magnetic near-fields and the Green's function to the scalar Helmholtz equation multiplied by a normal vector to the integration surface [34].

of resonance, respectively [see Fig. 2.2c)].

The shape of the radiation pattern of a 12.5 nm AuNP in the presence of a substrate, either embedded or supported, resembles that of the isolated 12.5 nm AuNP discussed in Section ?? [see Fig. ??] in that it follows a two-lobe and a one-lobe pattern depending on the orientation of \mathbf{E}^i relative to the scattering plane. If the incident electric field is parallel to the scattering plane, a two-lobe pattern aligned to the direction \mathbf{k}^i of the incident —and transmitted— plane wave arises as it can be seen in the Figs. 2.3a) and 2.3c) for the EE case, and Figs. 2.4a) and 2.4c) for the EI scenario. Contrastingly, when the incident electric field is perpendicular to the scattering plane, the one-lobe pattern can be identified [see Figs. 2.3b) and 2.3d) (SE), and 2.4b) and 2.4d) (SI)]. By comparing the Mie-limiting radiation pattern (see Fig. ??) with the radiation patterns considering a substrate, the later loses the polar symmetry observed in the Mie-limiting case. In particular, the amplitude of $\mathbf{E}_{\text{far}}^{\text{sca}}$ is larger when evaluated at the medium of incidence than at medium of transmission; this asymmetry is observed for both illuminating configurations

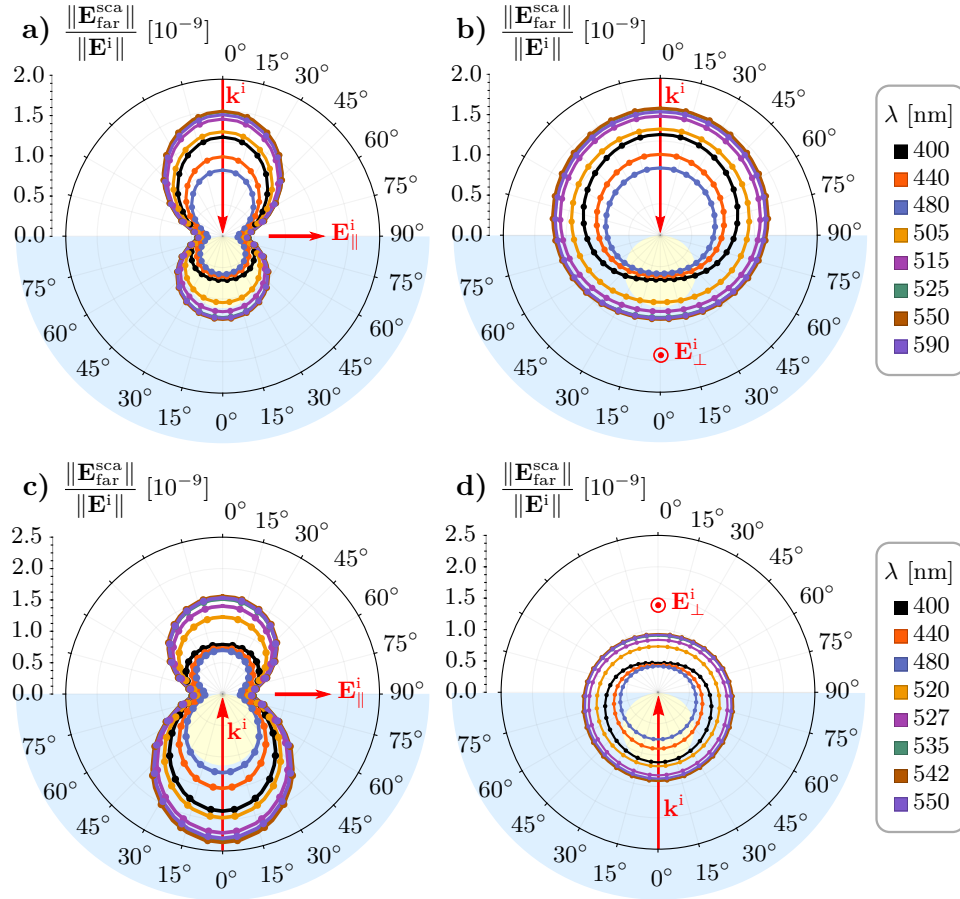


Fig. 2.3: Radiation patterns of a AuNP (light yellow) of radius $a = 12.5$ nm, embedded in a substrate (light blue) and illuminated by an electric plane wave \mathbf{E}^i with a wavelength λ , traveling in the \mathbf{k}^i direction normal to the interface between the substrate ($n_s = 1.5$) and the matrix ($n_m = 1$). The radiation patterns consider the illumination of the system **a,b**) in an external and **c,d**) in an internal configuration, and with an incident electric field **a,c**) \mathbf{E}_{\parallel}^i parallel to the scattering plane and **b,d**) \mathbf{E}_{\perp}^i perpendicular to it.

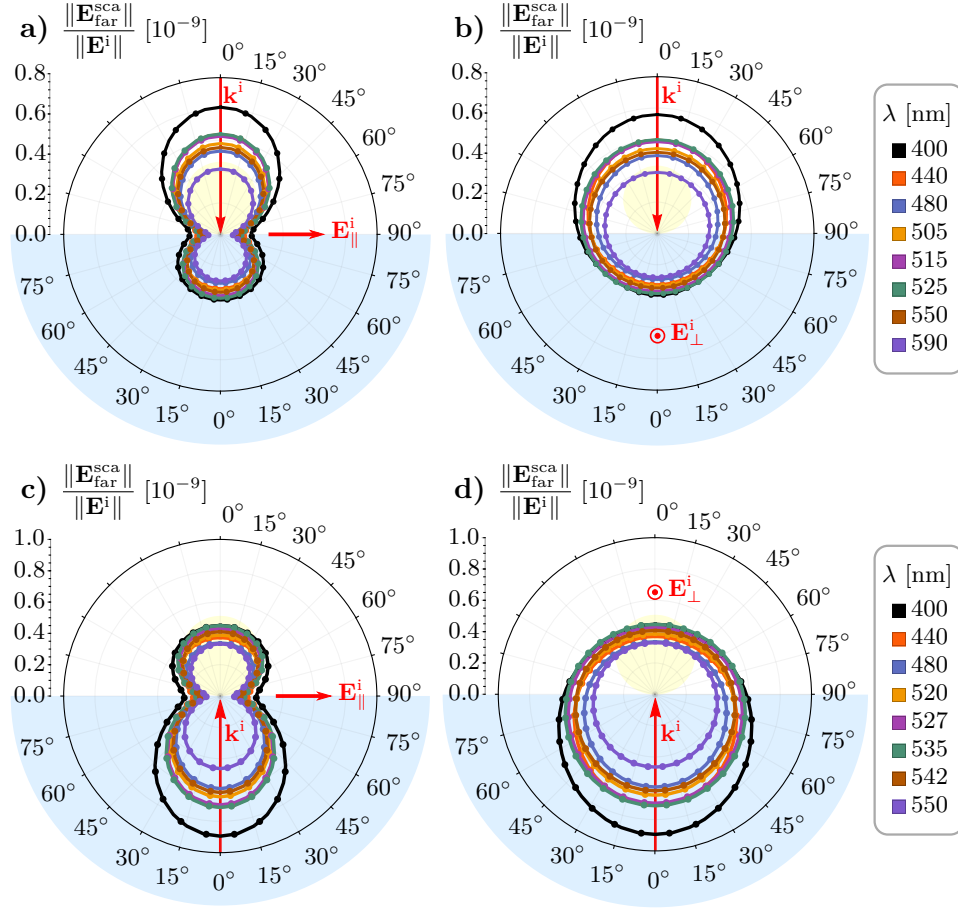


Fig. 2.4: Radiation patterns of a AuNP (light yellow) of radius $a = 12.5$ nm, supported on a substrate (light blue) and illuminated by an electric plane wave \mathbf{E}^i with a wavelength λ , traveling in the \mathbf{k}^i direction normal to the interface between the substrate ($n_s = 1.5$) and the matrix ($n_m = 1$). The radiation patterns consider the illumination of the system a,b) in an external and c,d) in an internal configuration, and with an incident electric field a,c) $\mathbf{E}^i_{||}$ parallel to the scattering plane and b,d) \mathbf{E}^i_{\perp} perpendicular to it.

(external and internal) and it does not depend on whether the AuNP is supported or embedded. Rather, the spatial configuration of the system determines the overall value of the far-field: when the AuNP is embedded, the far-field amplitude is greater by a factor of 2.5 than when the AuNP is supported—see the axis scale in Figs. 2.3 and 2.4—; this phenomenon is a consequence of the two following physical mechanisms. The first one is the substrate having a greater refractive index than the matrix, thus making the optical response of the 12.5 nm AuNP as that of a larger NP—but still small compared to the illuminating wavelength—, as in the Mie-limiting case. The second mechanism is the relative alignment of the electric point dipole induced within the AuNP—small particle approximation to the AuNP—and the induced electric dipole due to the interface, which is parallel when the AuNP is embedded into the substrate and antiparallel when supported on it, thus leading to a more energetic configuration when the AuNP is located inside the substrate than inside the matrix.

The radiation pattern, an optical property observed in the far-field regime, is a mani-

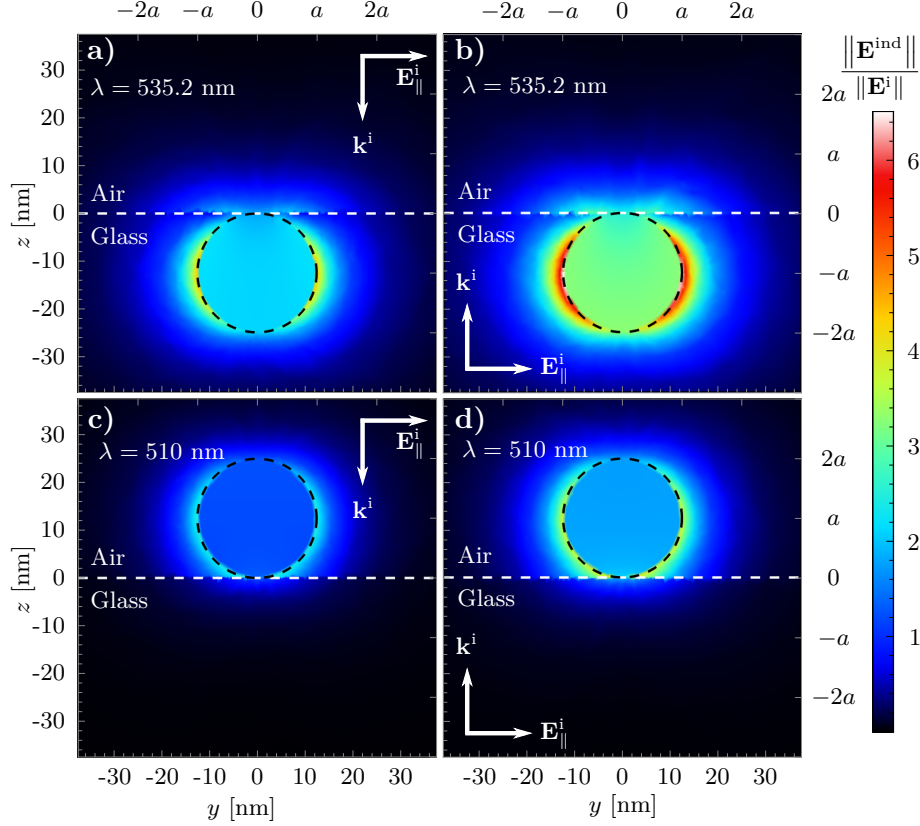


Fig. 2.5: Magnitude of the electric field induced \mathbf{E}^{ind} by a 12.5 nm AuNP (dashed black lines) illuminated by an incident electric plane wave \mathbf{E}^i traveling in the \mathbf{k}^i direction perpendicular to the interface (dashed white lines) between an air matrix ($n_m = 1$) and a glass substrate ($n_s = 1.5$) when the AuNP is **a,b**) embedded in the glass substrate and **c,d**) supported on it; the system is illuminated **a,c**) in an external and **b,d**) in an internal configuration at the resonance wavelength for the absorption efficiency.

festation of the near-field spatial distribution —see the footnote on page 10— which can be calculated numerically through the FEM for a AuNP of radius $a = 12.5$ nm. The scattered electric field in the far-field regime of a AuNP embedded or supported [Figs. 2.3 and 2.4] share some characteristics with the radiated field of an isolated AuNP (Mie-limiting case), and thus it should be for the near-field. In Fig. 2.5 it is shown the magnitude of the induced electric field \mathbf{E}^{ind} when the AuNP is illuminated by a y -polarized incident electric field \mathbf{E}^i traveling in the \mathbf{k}^i direction, perpendicular to the interface between air and glass; the induced electric field is evaluated at the scattering plane $x = 0$, that is, the incident electric field has only a parallel contribution \mathbf{E}_{\parallel}^i to the scattering plane. The wavelength λ of the incoming plane wave is $\lambda = 535.2$ nm for an embedded AuNP either illuminated externally [Fig. 2.5a)] or internally [Fig. 2.5b)] and $\lambda = 510$ nm for a supported AuNP either illuminated externally [Fig. 2.5c)] or internally [Fig. 2.5d)], which correspond to the wavelengths of the Localized Surface Plasmon Resonance (LSPR), that is, at the wavelength of maximum absorption.

The spatial distribution of the near-field shown in Fig. 2.5 is consistent with the description and explanation of both the absorption and scattering efficiencies [Figs. 2.2b) and 2.2c)] and the radiation patterns of the embedded [Fig. 2.3] and the supported [Fig. 2.4] AuNP. The induced

2. RESULTS AND DISCUSSION

electric field is, in general, stronger when the AuNP is embedded in the substrate than when it is supported on it, as can be seen in the magnitude of the hotspots around the AuNP: reddish regions in Figs. 2.5a) and 2.5b) and bluish in Figs. 2.5c) and 2.5d). These hotspots also verify that at the resonance wavelength, the main contribution to the electric fields is due to an electric dipolar moment since the characteristic two-lobe distribution of the near-field can be easily identified nevertheless, the lobes are not horizontally aligned to the AuNP's equator but farther from the substrate for the embedded AuNP and closer to it for the supported AuNP, as if the induced dipole—in the small particle approximation, where the AuNP is treated as an electric point dipole—is parallel (perpendicular) to the dipolar moment induced in the AuNP when it is embedded in (supported on) the substrate, as discussed above.

Throughout this Section, the optical properties of a 12.5 nm AuNP on the presence of a substrate considering four configurations were studied: the AuNP either embedded or supported and the system illuminated from under the substrate or from above. The choice of normal incidence to the system allowed the obtained results to be compared with the Mie-limiting case, which lead to the identification of similarities and differences among the four configurations. The differences in the optical response are associated to the broken symmetry due to the two semiinfinite media now considered [31], while the similarities arise since the system is always illuminated by a plane wave independently of the choice of the medium of incidence, yielding a mostly dipolar electric field. Therefore, in the next Section the oblique incidence case is addressed only when the AuNP is supported and illuminated in the internal configuration, since it is the only case with a different type illumination to the system: an evanescent wave for incidence angles above the critical angle $\theta_c = \arcsin(n_m/n_s)$ [35].

Conclusions

In this thesis, the optical properties of a spherical gold nanoparticle (AuNP) of radius $a = 12.5$ nm, partially embedded in an air matrix and in a glass substrate, was studied as a function of its embedding degree, characterized by the incrustation parameter h/a —with h the position of the center of the AuNP relative to the planar air-glass interface—. By means of the Finite Element Method —implemented in the commercial software COMSOL Multiphysics™ Ver. 5.4— the absorption and scattering efficiencies, the radiation pattern and the spatial distribution of the induced electric field of the partially embedded 12.5 nm AuNP were calculated when the AuNP was illuminated by an electromagnetic plane wave traveling at an oblique direction, with a defined polarization state; all numerical results were compared with the Mie-limiting cases calculated analytically, consisting in a 12.5 nm AuNP embedded in an infinite matrix of air, and an infinite matrix of glass. From the preformed calculations, it was observed that the 12.5 nm AuNP with partial embedding can be described by a mainly dipolar contribution, that its coupling with the incident light and the spatial distribution of the electric field enhancement on its surface can be tuned depending on the embedding of the AuNP and its illumination conditions, and that the optical response is maximized if the system is illuminated with an evanescent wave at an angle of incidence near the critical angle. More specifically, from the preformed calculations the following can be concluded:

- **The optical response of a single partially embedded AuNP can be described by a mainly dipolar contribution.**

The absorption and scattering efficiencies present only one global maximum in the visible spectrum, at which the spatial distribution of the electric field enhancement and its radiation pattern resemble that of an electric point dipole. This behavior can be extended to other materials of the matrix, the substrate and the nanosphere (of any size) as long as the scattering contribution to the extinction of light is small compared to the absorption contribution.

- **There is a smooth transition between the two Mie-limiting cases as the nanosphere is partially embedded into the substrate.**

The wavelength of resonance of the absorption and scattering efficiencies of the partially embedded nanosphere is localized in between the two Mie-limiting cases, which consist in the nanosphere embedded in an infinite media (either the matrix or the substrate). Additionally, the wavelength of resonance is redshifted from the resonance wavelength of the matrix Mie-limiting case to the resonance wavelength of the substrate Mie-limiting case, and this redshift is different for an s or for a p polarized incident electric field.

- **The optical response of the nanosphere resembles that of a supported (totally embedded) nanosphere if at most one eighth of its volume is partially embedded in the substrate (matrix).**

The supported and totally embedded nanosphere are the extreme cases of the partially embedded nanosphere when the sphere is tangential to the matrix-substrate interface. The absorption and scattering efficiencies of the partially embedded nanospheres, for both polarizations, are enhanced and redshifted in the same trend as the supported and totally embedded spheres as the angle of incidence of the incident light changes if at most one eighth of the nanosphere crossed the interface.

- **The optical properties of the partially embedded nanospheres are maximized if illuminated at an angle of incidence near the critical angle.**

For any incrustation parameter and polarization state, the magnitude of the scattering and absorption efficiencies is enhanced—for all wavelengths in the visible spectrum—as the angle of incidence grows from zero to the critical angle, and they start to diminish for angles of incidence above the critical angle. This behavior is due to the effect of an evanescent wave illuminating the system above the interface, whose penetration depth is maximum at the critical angle.

- **The wavelength of resonance and the electric field spatial distribution of the partially embedded nanospheres for s polarized illumination do not depend on the angle of incidence while they do for p polarized illumination.**

On the one hand, for s polarization, the redshift of the resonance wavelength as the nanosphere is buried into the substrate, is the same for all angles of incidence and the electric field at the resonance wavelength is enhanced in two hotspots aligned parallel to the interface and on the surface of the nanosphere in the substrate side of the system. On the other hand, for p polarization, the redshift of the resonance wavelength is different for each angle of incidence. For example, near the critical angle, the redshift is appreciable if more than half of the nanosphere is buried into the substrate, while for normal incidence the behavior is equivalent to the s polarization case. On the spatial distribution, one hotspot is located in the matrix and other in the substrate, and their alignment is determined by the transmitted electric field; in particular, for angles above the critical angle, the hotspots are aligned perpendicular to the substrate.

Finally, it can be concluded that the optical properties of a partially embedded spherical AuNP of radius 12.5 nm, with at most one eighth of its volume buried into the substrate, is suited for interactions with elements in the matrix under internal illumination. If the system is illuminated with a p polarized incident electromagnetic plane wave traveling at an angle $\theta_i \gtrsim \theta_c$, the system is optimized to interact with its surroundings above the substrate since the optical response is maximized in the matrix. Therefore, partially embedded spherical AuNPs are strong candidates for meta-atoms conforming a disordered biosensing-aimed-metasurface.

Bibliography

- [1] S. A. Khan, N. Z. Khan, Y. Xie, M. T. Abbas, M. Rauf, I. Mehmood, M. Runowski, S. Agathopoulos, and J. Zhu. Optical sensing by metamaterials and metasurfaces: from physics to biomolecule detection. *Advanced Optical Materials*, **10**(18):2200500, 2022. DOI: [10.1002/adom.202200500](https://doi.org/10.1002/adom.202200500).
- [2] A. K. González-Alcalde and A. Reyes-Coronado. Large angle-independent structural colors based on all-dielectric random metasurfaces. *Optics Communications*, **475**:126289, 2020. DOI: [10.1016/j.optcom.2020.126289](https://doi.org/10.1016/j.optcom.2020.126289).
- [3] M. Kim, J. Lee, and J. Nam. Plasmonic photothermal nanoparticles for biomedical applications. *Advanced Science*, **6**(17):1900471, 2019. DOI: [10.1002/advs.201900471](https://doi.org/10.1002/advs.201900471). (Visited on 10/27/2022).
- [4] H.-T. Chen, A. J. Taylor, and N. Yu. A review of metasurfaces: physics and applications. *Reports on Progress in Physics*, **79**(7):076401, 2016. DOI: [10.1088/0034-4885/79/7/076401](https://doi.org/10.1088/0034-4885/79/7/076401).
- [5] M.-C. Estevez, M. A. Otte, B. Sepulveda, and L. M. Lechuga. Trends and challenges of refractometric nanoplasmonic biosensors: a review. *Analytica Chimica Acta*, **806**:55–73, 2014. DOI: [10.1016/j.aca.2013.10.048](https://doi.org/10.1016/j.aca.2013.10.048).
- [6] P. K. Jain, X. Huang, I. H. El-Sayed, and M. A. El-Sayed. Noble metals on the nanoscale: optical and photothermal properties and some applications in imaging, sensing, biology, and medicine. *Accounts of Chemical Research*, **41**(12):1578–1586, 2008. DOI: [10.1021/ar7002804](https://doi.org/10.1021/ar7002804).
- [7] A. V. Kabashin, P. Evans, S. Pastkovsky, W. Hendren, G. A. Wurtz, R. Atkinson, R. Pollard, V. A. Podolskiy, and A. V. Zayats. Plasmonic nanorod metamaterials for biosensing. *Nature Materials*, **8**(11):867–871, 2009. DOI: [10.1038/nmat2546](https://doi.org/10.1038/nmat2546).
- [8] L. Feuz, P. Jönsson, M. P. Jonsson, and F. Höök. Improving the limit of detection of nanoscale sensors by directed binding to high-sensitivity areas. *ACS Nano*, **4**(4):2167–2177, 2010. DOI: [10.1021/nn901457f](https://doi.org/10.1021/nn901457f).
- [9] G. Qiu, Z. Gai, Y. Tao, J. Schmitt, G. A. Kullak-Ublick, and J. Wang. Dual-functional plasmonic photothermal biosensors for highly accurate severe acute respiratory syndrome coronavirus 2 detection. *ACS Nano*, **14**(5):5268–5277, 2020. DOI: [10.1021/acsnano.0c02439](https://doi.org/10.1021/acsnano.0c02439).
- [10] M. Svedendahl, R. Verre, and M. Käll. Refractometric biosensing based on optical phase flips in sparse and short-range-ordered nanoplasmonic layers. *Light: Science & Applications*, **3**(11):e220–e220, 2014. DOI: [10.1038/lsa.2014.101](https://doi.org/10.1038/lsa.2014.101).

- [11] Q. K. Hammad, A. N. Ayyash, and F. A.-H. Mutlak. Improving SERS substrates with au/ag-coated si nanostructures generated by laser ablation synthesis in PVA. *Journal of Optics*, **52**(3):1528–1536, 2023. DOI: [10.1007/s12596-022-00971-4](#).
- [12] D. Wang, R. Ji, and P. Schaaf. Formation of precise 2d au particle arrays via thermally induced dewetting on pre-patterned substrates. *Beilstein Journal of Nanotechnology*, **2**:318–326, 2011. DOI: [10.3762/bjnano.2.37](#).
- [13] G. Qiu, S. P. Ng, and C. M. L. Wu. Differential phase-detecting localized surface plasmon resonance sensor with self-assembly gold nano-islands. *Optics Letters*, **40**(9):1924, 2015. DOI: [10.1364/OL.40.001924](#).
- [14] A. Reyes-Coronado, G. Pirruccio, A. K. González-Alcalde, J. A. Urrutia-Anguiano, A. J. Polanco-Mendoza, G. Morales-Luna, O. Vázquez-Estrada, A. Rodríguez-Gómez, A. Issa, S. Jradi, et al. Enhancement of light absorption by leaky modes in a random plasmonic metasurface. *The Journal of Physical Chemistry C*, **126**(6):3163–3170, 2022. DOI: [10.1021/acs.jpcc.1c08325](#).
- [15] G. Bosi. Transmission of a thin film of spherical particles on a dielectric substrate: the concept of effective medium revisited. *Journal of the Optical Society of America B*, **9**(2):208, 1992. DOI: [10.1364/JOSAB.9.000208](#).
- [16] R. G. Barrera, M. del Castillo-Mussot, G. Monsivais, P. Villaseor, and W. L. Mochán. Optical properties of two-dimensional disordered systems on a substrate. *Phys. Rev. B*, **43**(17):13819–13826, 1991. DOI: [10.1103/PhysRevB.43.13819](#) (cited on pages [1](#), [10](#)).
- [17] D. Bedeaux and J. Vlieger. *Optical properties of surfaces*. Imperial College Press, London, 2nd edition, 2004. 450 pages. ISBN: 978-1-86094-450-5.
- [18] M. Svedendahl and M. Käll. Fano interference between localized plasmons and interface reflections. *ACS Nano*, **6**(8):7533–7539, 2012. DOI: [10.1021/nl302879j](#). Number: 8.
- [19] A. Sihvola. *Electromagnetic Mixing Formulas and Applications*. Electronic Waves. The Institution of Engineering and Technology, 2008. ISBN: 978-0-85296-772-0.
- [20] O. Vázquez-Estrada and A. García-Valenzuela. Optical reflectivity of a disordered monolayer of highly scattering particles: coherent scattering model versus experiment. *Journal of the Optical Society of America A*, **31**(4):745, 2014. DOI: [10.1364/JOSAA.31.000745](#). Number: 4 (cited on pages [5](#), [6](#)).
- [21] A. Reyes-Coronado, G. Morales-Luna, O. Vázquez-Estrada, A. García-Valenzuela, and R. G. Barrera. Analytical modeling of optical reflectivity of random plasmonic nano-monolayers. *Optics Express*, **9594**:6697–6706, 2018. DOI: [10.1364/OE.26.012660](#) (cited on page [1](#)).
- [22] C. Noguez. Surface Plasmons on Metal Nanoparticles: The Influence of Shape and Physical Environment. *The Journal of Physical Chemistry C*, **111**(10):3806–3819, 2007. DOI: [10.1021/jp066539m](#).
- [23] L. J. Mendoza Herrera, D. M. Arboleda, D. C. Schinca, and L. B. Scaffardi. Determination of plasma frequency, damping constant, and size distribution from the complex dielectric function of noble metal nanoparticles. *Journal of Applied Physics*, **116**(23):233105, 2014. DOI: [10.1063/1.4904349](#).
- [24] J. Barzilai and J. M. Borwein. Two-point step size gradient methods. *IMA Journal of Numerical Analysis*, **8**(1):141–148, 1988. DOI: [10.1093/imanum/8.1.141](#).
- [25] V. A. Loiko, V. P. Dick, and V. I. Molochko. Monolayers of discrete scatterers: comparison of the single-scattering and quasi-crystalline approximations. *Journal of the Optical Society of America A*, **15**(9):2351, 1998. DOI: [10.1364/JOSAA.15.002351](#) (cited on pages [1](#), [3](#)).

- [26] R. G. Barrera and A. García-Valenzuela. Coherent reflectance in a system of random mie scatterers and its relation to the effective-medium approach. *Journal of the Optical Society of America A*, **20**(2):296, 2003. DOI: [10.1364/JOSAA.20.000296](https://doi.org/10.1364/JOSAA.20.000296) (cited on pages 1–5).
- [27] A. García-Valenzuela, E. Gutiérrez-Reyes, and R. G. Barrera. Multiple-scattering model for the coherent reflection and transmission of light from a disordered monolayer of particles. *JOSA A*, **29**(6):1161–1179, 2012. DOI: [10.1364/JOSAA.29.001161](https://doi.org/10.1364/JOSAA.29.001161) (cited on pages 1–5).
- [28] L. Tsang, J. A. Kong, and K.-H. Ding. *Scattering of Electromagnetic Waves: Theories and Applications*. John Wiley & Sons, Inc., New York, USA, 2000. ISBN: 978-0-471-22428-0 978-0-471-38799-2. DOI: [10.1002/0471224286](https://doi.org/10.1002/0471224286) (cited on page 2).
- [29] C. F. Bohren and D. R. Huffman. *Absorption and Scattering of Light by Small Particles*. Wiley Science Paperbak Series. John Wiley & Sons, 1st edition, 1983. ISBN: 0-471-029340-7 (cited on page 4).
- [30] P. B. Johnson and R. W. Christy. Optical Constants of the Noble Metals. *Physical Review B*, **6**(12):4370–4379, 1972. DOI: [10.1103/PhysRevB.6.4370](https://doi.org/10.1103/PhysRevB.6.4370) (cited on pages 7, 8).
- [31] X. Meng, T. Shibayama, R. Yu, J. Ishioka, and S. Watanabe. Anisotropic surroundings effects on photo absorption of partially embedded au nanospheroids in silica glass substrate. *AIP Adv*, **5**(2):027112, 2015. DOI: [10.1063/1.4908010](https://doi.org/10.1063/1.4908010) (cited on pages 10, 14).
- [32] COMSOL Multiphysics™ Ver. 6.0. *Wave Optics Module User’s Guide*. <https://doc.comsol.com/5.4/doc/com.comsol.help.woptics/WaveOpticsModuleUsersGuide.pdf>. COMSOL AB. Stockholm, Sweden., 2021 (cited on page 10).
- [33] N. V. Anyutin, K. I. Kurbatov, I. M. Malay, and M. A. Ozerov. Algorithm for transforming antenna electromagnetic near-field measured on spherical surface into far-field based on direct calculation of Stratton and Chu formulas. *Radioelectronics and Communications Systems*, **62**(3):109–118, 2019. DOI: [10.3103/S0735272719030026](https://doi.org/10.3103/S0735272719030026) (cited on page 10).
- [34] J. A. Stratton and L. J. Chu. Diffraction theory of electromagnetic waves. *Physical Review*, **56**(1):99–107, 1939. DOI: [10.1103/PhysRev.56.99](https://doi.org/10.1103/PhysRev.56.99) (cited on page 10).
- [35] M. Born and W. Emil. *Principle of Optics: Electromagnetic Theory of Propagation, Interference and Diffraction of Light*. Cambridge University Press, New York, USA, 7th edition, 1999. ISBN: 0-521-64222-1 (cited on page 14).